Evolution of lattice, spin, and charge properties across the phase diagram of FeSe$_{1-x}$S$_x$

N. Lazarević [1,*], A. Baum,[2,3,*] A. Milosavljević,[1] L. Peis [2,3,†] R. Stumberger,[2,3,‡] J. Bekaert [4] A. Šolajić,[1] J. Pešić [1]
Aifeng Wang,[5] M. Šćepanović,[1] A. M. Milinda Abeykoon,[6] M. V. Milošević,[4] C. Petrovic,[7] Z. V. Popović,[1,8] and R. Hackl[2,3,9]

[1]*Center for Solid State Physics and New Materials, Institute of Physics Belgrade,*
University of Belgrade, Pregrevica 118, 11080 Belgrade, Serbia
[2]*Walther Meissner Institut, Bayerische Akademie der Wissenschaften, 85748 Garching, Germany*
[3]*Fakultät für Physik, Technische Universität München, 85478 Garching, Germany*
[4]*Department of Physics, University of Antwerp, Groenenborgerlaan 171, B-2020 Antwerp, Belgium*
[5]*School of Physics, Chongqing University, Chongqing 400044, China*
[6]*National Synchrotron Light Source II, Brookhaven National Laboratory, Upton, New York 11973, USA*
[7]*Condensed Matter Physics and Materials Science Department, Brookhaven National Laboratory, Upton, New York 11973-5000, USA*
[8]*Serbian Academy of Sciences and Arts, Kneza Mihaila 35, 11000 Belgrade, Serbia*
[9]*IFW Dresden, Helmholtzstr. 20, 01069 Dresden, Germany*

A Raman scattering study covering the entire substitution range of the FeSe$_{1-x}$S$_x$ solid solution is presented. Data were taken as a function of sulfur concentration x for $0 \leqslant x \leqslant 1$, of temperature and of scattering symmetry. All types of excitations including phonons, spins, and charges are analyzed in detail. It is observed that the energy and width of the iron-related B_{1g} phonon mode vary continuously across the entire range of sulfur substitution. The A_{1g} chalcogenide mode disappears above $x = 0.23$ and reappears at a much higher energy for $x = 0.69$. In a similar way the spectral features appearing at finite doping in A_{1g} symmetry vary discontinuously. The magnetic excitation centered at approximately 500 cm^{-1} disappears above $x = 0.23$ where the A_{1g} lattice excitations exhibit a discontinuous change in energy. The low-energy mode associated with fluctuations displays maximal intensity at the nematostructural transition and thus tracks the phase boundary.

I. INTRODUCTION

Iron-based compounds are widely believed to host unconventional superconductivity, thus being similar to cuprates or heavy fermion systems. All are characterized by competing phases including magnetism, crystal symmetry breaking or nematicity, and fluctuations of charge and spin prior to superconductivity [1–3]. While long-range magnetic ordering was found in the majority of the compounds, it is absent in the binary compound FeSe. Yet a nematic and structural phase transition occurs simultaneously at 90 K [4–6]. Below $T_c = 9$ K superconductivity is observed [7]. Upon applied pressure T_c increases to approximately 37 K [8]. By substituting sulfur for selenium, the transition temperature to the nematic phase is suppressed to zero for $x \sim 0.2$ [9], suggesting the existence of a quantum critical point (QCP), and a depression of T_c to approximately 2 K. For $x > 0.2$, T_c increases again and

reaches 5 K at $x = 1$ [10]. Surprisingly enough, FeS displays a metallic variation of the resistivity and a high residual resistivity ratio RRR of approximately 30, and neither structural nor nematic phase transitions occur [11]. Thus, FeSe$_{1-x}$S$_x$ uniquely offers access to instabilities and critical points and the disappearance thereof while superconductivity survives.

FeSe and FeS are isostructural, thus providing us with the opportunity to probe the evolution of competing order by isoelectronic substitution. We wish to address the question as to which extent the properties and, specifically, superconductivity are interrelated with the other instabilities and how the electronic properties affect the phonons. We employ inelastic light scattering to probe evolution with composition of lattice spin and charge excitations in FeSe$_{1-x}$S$_x$ [12]. We identify the A_{1g} and B_{1g} modes, a two-phonon scattering process as well as additional modes that can be traced to either defect-induced or second-order scattering. The obtained experimental results are in good agreement with numerical calculations. Phonons self-energy temperature dependence supports the results reported in Refs. [13,14] where emerging short-range magnetic order at approximately 20 K was reported.

II. EXPERIMENT

Single crystals of FeSe$_{1-x}$S$_x$ were synthesized as described elsewhere [15]. Before the experiment the samples were cleaved in air.

Inelastic light scattering on phonons was performed using a Tri Vista 557 Raman spectrometer with the first

---

*These authors contributed equally to this work.

†Present Address: IFW Dresden, Helmholtzstr. 20, 01069 Dresden, Germany.

‡Present Address: Robert Bosch GmbH, Robert-Bosch-Platz 1, 70839 Gerlingen, Germany.
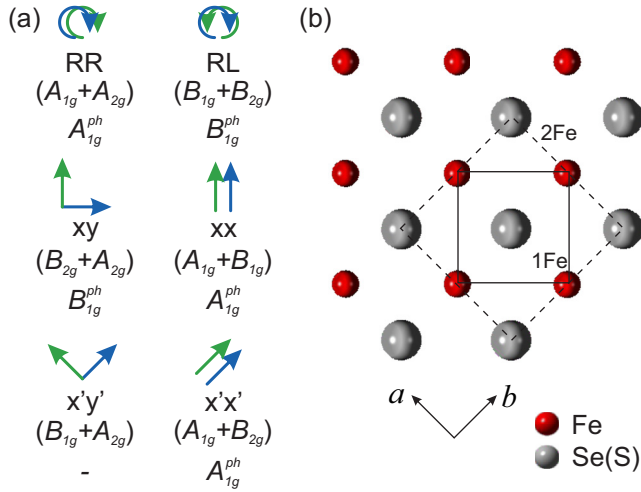
FIG. 1. Crystal structure and selection rules for FeSe(S). Solid and dashed lines represent the 1-Fe and the crystallographic 2-Fe unit cell, respectively. The crystallographic axes are a and b. In FeSe and FeS only one A_{1g} and one B_{1g} phonon is expected as indicated by A_{1g}^{ph} and B_{1g}^{ph}, respectively. The symmetries projected with the polarizations indicated symbolically with respect to the 1-Fe cell are relevant for electronic and spin excitations. The symmetries of the phonons are in brackets.

two monochromators coupled subtractively and the grating combination 1800/1800/2400 grooves/mm. For excitation a Coherent Verdi G solid state laser was used emitting at 532 nm. The samples were mounted in a KONTI CryoVac continuous helium flow cryostat having a 0.5-mm-thick window. The vacuum was pumped to the range of 10^{-6} mbar using a turbo molecular pump. The laser was focused to a spot size of approximately 8 μm using a microscope objective lens with $\times 50$ magnification. The power absorbed by the sample was $P_a = 0.75$ mW. In backscattering configuration as used here, the incident and scattered photons propagate parallel to the crystallographic c axis. All Raman spectra were divided by the Bose factor.

Fluctuations and two magnon excitations were probed with a calibrated scanning spectrometer. The samples were attached to the cold finger of a He-flow cryostat having a vacuum of better than 10^{-6} mbar. A diode-pumped solid state laser emitting at 575 nm (Coherent GENESIS) was used as an excitation source. The laser beam was focused on the sample at an angle of incidence of 66° to a spot of $2r_f \approx 50$ μm. Polarization and power of the incoming light were adjusted in a way that the light inside the sample had the proper polarization state and a power of $P_a = 4$ mW independent of polarization. The ratio P_a/r_f is similar for the μ setup and thus the local heating for both experiments can be estimated to be in the range 3–5 K. All four symmetries of the D_{4h} group, A_{1g}, A_{2g}, B_{1g}, and B_{2g}, can be accessed using appropriate in-plane polarizations of the incident and scattered light.

The selection rules are dictated by the crystal structure. Here, only polarizations in the ab plane are relevant, as shown in Fig. 1, with solid and dashed lines representing 1-Fe and 2-Fe unit cells, respectively. For the tetragonal system there are six principal scattering geometries and each probes two symmetry channels. We align our laboratory system with the
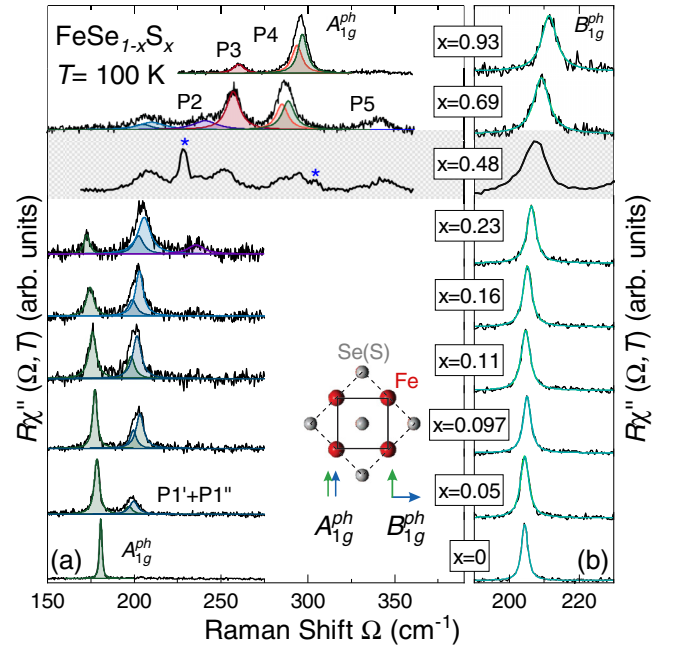
FIG. 2. Phonon spectra of FeSe$_{1-x}$S$_x$ measured at 100 K. We show xx and xy spectra where x and y are rotated by 45° with respect to the 2-Fe unit cell, as indicated in the inset, and project A_{1g}^{ph} and B_{1g}^{ph}, respectively. (a) A_{1g}^{ph} spectra. Only for pure FeSe ($x = 0$), a single line is observed at the A_{1g} energy of 165 cm^{-1} expected from lattice dynamics. Above $x = 0.23$ the Se(S) vibration becomes unobservable and reappears only for $x \geqslant 0.69$ at a much higher energy of approximately 290 cm^{-1} similar to that in pure FeS. The spectrum at $x = 0.48$ was measured on the scanning spectrometer and is therefore shaded. There may be an indication of the A_{1g}^{ph} phonon at about 290 cm^{-1}. The peaks other than Raman-active phonons are labeled P1–P5 with increasing energy. Those with asterisks correspond to maxima in the phonon density of states (Fig. 6). Solid lines represent the best fits to the data using Voigt profiles. (b) B_{1g}^{ph} spectra. Energy and linewidth vary continuously with sulfur content.

1-Fe unit cell. As a consequence, the B_{1g} phonon (B_{1g}^{ph}) is observable in the xy configuration which corresponds to the B_{2g} symmetry channel in the 2-Fe cell (Fig. 1). We decided to use this orientation since our main focus here is electronic and spin excitations for which the 1-Fe unit cell is more appropriate. A_{1g}^{ph} is the fully symmetric in-phase Se(S) mode with elongations along the c axis; B_{1g}^{ph} corresponds to the out-of-phase vibration of the Fe atoms parallel to the c axis.

III. RESULTS AND DISCUSSION

A. Lattice excitations

First, the focus is placed on lattice excitations observable in the xx and xy scattering configuration projecting A_{1g}^{ph} and B_{1g}^{ph} in the spectral range characteristic for phonons. Figure 2 shows the evolution of the spectra with doping x, where x indicates the sulfur concentration. Additional spectra for $x = 0.48$ and, for convenience, $x = 1$ are shown in Fig. 7. In order to minimize the thermal broadening of the modes while staying above the nematic phase transition, the spectra
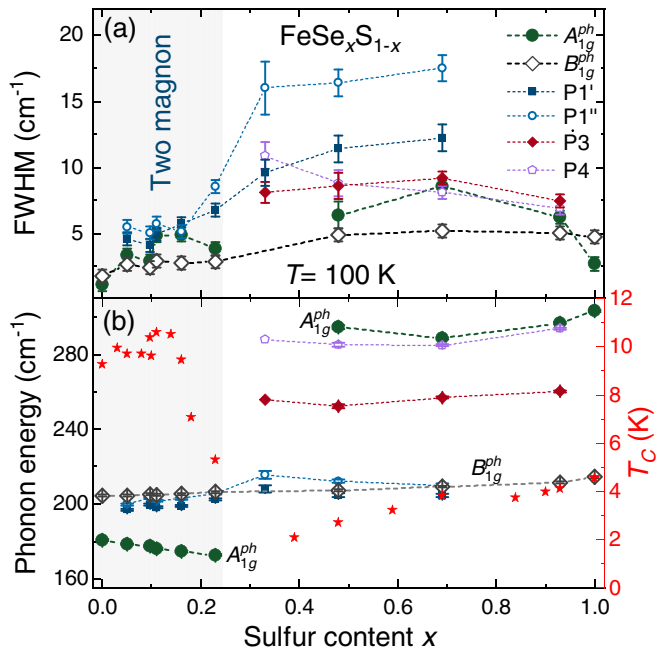
FIG. 3. Energies and linewidths of the Raman-active modes and T_c in FeSe$_{1-x}$S$_x$ as a function of sulfur content x at 100 K. (a) Peak widths (FWHM) and (b) energies as obtained from the fits (left axis). The T_c values of the corresponding solid solution are taken from Ref. [16].

were recorded at 100 K. In pure stoichiometric compounds only one A_{1g}^{ph} and one B_{1g}^{ph} phonon mode is expected (see Fig. 1). This is indeed the case for FeSe [Fig. 2(a), bottom] as described by Gnezdilov *et al.* [17] and corroborated here. In contrast, in pure FeS ($x = 1$) additional modes exist in the *xx* spectrum which were assigned to two-phonon scattering (265 cm^{-1}) and a projection of the phonon density of states (PDOS) ($\sim$300 cm^{-1}) [18] as reproduced in Fig. 7(b). The *xy* spectra show only the B_{1g}^{ph} mode for all doping levels displayed here [see also Fig. 7(a)]. It hardens monotonously and exhibits a weak maximum of the linewidth at $x = 0.69$ and $x = 0.93$ highlighting the effect of disorder as summarized in Figs. 3(a) and 3(b).

The *xx* spectra display a much more complex doping dependence. Upon substituting only a small amount of sulfur ($x = 0.05$) for selenium an additional structure appears at about 200 cm^{-1} [Fig. 2(a)]. Closer inspection of the FeSe$_{0.95}$S$_{0.05}$ spectra reveals that this feature consists of two peaks denoted as P1$'$ and P1$''$. With increasing x, these structures gain intensity and harden slightly, whereas the A_{1g} phonon softens, gradually loses intensity, and becomes undetectable at concentrations above $x = 0.23$. It reappears as a clear peak only for $x \geqslant 0.69$ at a much higher energy characteristic for FeS [18] and possibly as a remnant structure in the spectrum for $x = 0.48$ [Fig. 7(a)]. As in FeS the A_{1g}^{ph} peak overlaps with a weaker structure which is compatible with the PDOS (P4). At $x = 0.69$ P4 is approximately as strong as the A_{1g} phonon. Here [and at $x = 0.48$, Fig. 7(a)] there is also a broad feature at 340 cm^{-1} (P5). For $x = 0.93$ similar to $x = 1$ there is another structure at 250 cm^{-1} (P3) which gains intensity toward $x = 0.69$ where it has a weak companion at

235 cm^{-1} (P2) being present down to $x = 0.23$. As expected, the increase of crystalline disorder due to substitution leads to a broadening of all observed modes to some maximum value before the trend reverses for compositions close to pure FeS. The widths and energies of the stronger modes are summarized in Fig. 3. As opposed to the B_{1g}^{ph} phonon in *xy* configuration, all modes in *xx* polarization including the Raman-active phonon depend quasidiscontinuously on substitution.

This dichotomy of the substitution dependence of the phonon part in *xx* and *xy* configuration is the most remarkable effect of this study. Whereas the continuous evolution of the Fe B_{1g} line by and large tracks the degree of disorder and lattice contraction, the Se/S A_{1g} mode varies counterintuitively. Naively one would expect a continuous (not necessarily trivial) increase in the phonon frequency and maximal broadening for doping levels around $x = 0.5$ similar to what is observed in isotopically substituted semiconductors [19]. However, the line disappears after a continuous loss of intensity at approximately $x = 0.23$ and 172 cm^{-1} and reappears (presumably) at $x = 0.48$ slightly below 300 cm^{-1}. At low doping the A_{1g} energy decreases by 4% although S is lighter than Se by a factor of 2.13 and the lattice contracts. Above $x = 0.48$ the energy of the A_{1g} phonon varies as expected [see Fig. 3(b)].

The structures appearing in addition to the allowed phonons are rather difficult to interpret in detail. There are essentially two possibilities for intensity to appear in addition to the phonons: defect-induced scattering projecting the PDOS on the site of the defect or overtone (combination) scattering [20]. In FeS one of the peaks (P3) is in the gap between the acoustic and the optical branches and was therefore assigned to an overtone, whereas P4 may originate from the PDOS [18]. The two features depend in the same fashion on doping as the A_{1g} phonon, and the assignment may be maintained. This is plausible on the basis of the PDOS (Fig. 6) although the PDOS of a solid solution cannot be calculated straightforwardly. If we argue that the extra lines vary as discontinuously as the phonon, P1$'$ and P1$''$ would have both an overtone and a PDOS component. Interestingly, P1$'$ and P1$''$ have the expected doping dependence [see Fig. 3(b)].

The anomalous doping dependence of the A_{1g} phonon may indicate an enhanced electron-phonon coupling which manifests itself also in the linewidth (on top of the inhomogeneous broadening) [Fig. 3(a)]. The slightly enhanced electron-phonon coupling may boost T_c a little bit until the structure becomes unstable and T_c decreases rapidly for $x > 0.16$. There is, in fact, a kink in the c/a ratio at $x = 0.23$ which may be related to the structural instability [15]. In a recent preprint the collapse of T_c is almost precipitous and coincides with the end of the nematic phase [21], and one may speculate about the position of the quantum critical point and its impact. Yet, further work is necessary to finally clarify the issue.

B. Spin excitations and fluctuations

Second, we focus on the electronic B_{1g} symmetry channel projected in the $x'y'$ (1-Fe) configuration. Figure 4 shows the doping dependence of the high-energy Raman spectra at approximately 4 K. The A_{2g} contribution can be neglected in these materials [22]. A broad excitation centered at about
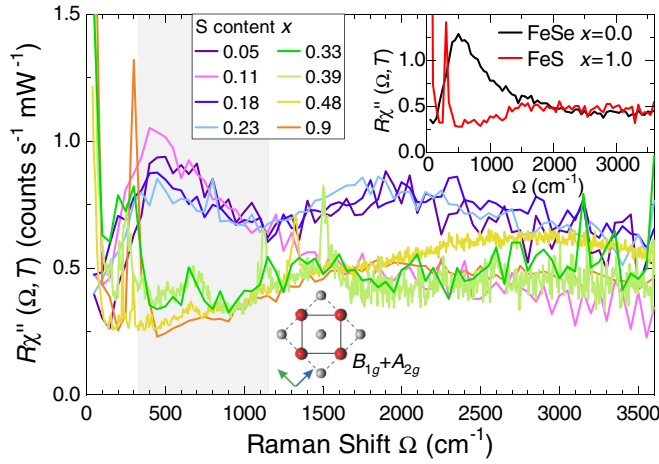
FIG. 4. Doping dependence of the high-energy spectra of FeSe$_{1-x}$S$_x$ in xy (2-Fe) configuration at 4 K, except for $x = 0.33$, $x = 0.39$, and $x = 0.48$ which were obtained at 100 K. For the electronic unit cell (full line in Fig. 1) relevant here the B_{1g} and A_{2g} symmetries are projected where A_{2g} is negligibly weak. The doping levels are indicated. The inset compares the high-energy spectra of pure FeSe [22] and FeS. The maximum in the range 500 cm^{-1} is compatible with two-magnon scattering [23], whereas the broad shoulder around 2000 cm^{-1} appearing in three out of ten (including all doping levels) spectra was identified as luminescence by using various laser lines for excitation. The peaks in the range 700–1550 cm^{-1} observed only for the doping levels $x = 0.33$, $x = 0.39$, and $x = 0.48$ may originate from either overtones of the phonon density of states [20,24] or from magnetic excitations in the paramagnetic state above the magnetic phase which was observed recently below 20–40 K [25,26]. Since the measuring temperature is well above the magnetic transition the former is more likely.

500 cm^{-1} dominates the spectrum at $x = 0$ which was interpreted in terms of two-magnon scattering [22]. Since the ratio of the nearest to the next-nearest-neighbor exchange coupling $J1$ and $J2$ is close to 0.5 [27] the system is a nearly frustrated antiferromagnet. Consequently the two-magnon Raman peak is pushed to energies well below $3J1$ [23]. No comparable feature is observed in FeS (see inset in Fig. 4).

Upon doping, the two-magnon peak remains relatively robust up to $x = 0.23$ and is absent for higher doping levels. This goes in line with the fact that for $x = 0$, the Fermi velocity in the d_{xy} band, $v_F^{(xy)}$, is significantly smaller than $v_F^{(xz)}$ or $v_F^{(yz)}$ and increases by only 10% for $x \leqslant 0.20$. For $x > 0.20$ $v_F^{(xy)}$ increases significantly towards FeS [28]. Generally, $v_F^{(xy)}$ in FeSe is smaller than $v_F^{(xy)}$ in Ba(Fe$_{1-x}$Co$_x$)$_2$As$_2$ for instance [29], in agreement with theoretical predictions [30–32]. Thus FeSe is close to the localization limit, and the two-magnonlike response may result from the rather slow carriers on the d_{xy} band. In contrast, the more itinerant carriers in the pnictides condense into a stripelike spin density wave (SDW) which becomes manifest in a gap and a coherence peak [22,33].

In the energy region $\Omega < 200$ cm^{-1} extra intensity is observed for low temperatures. In FeSe it becomes clearly visible below 200 K and fills the spectral gap below the magnon at 500 cm^{-1}. Below approximately 100 K an isolated
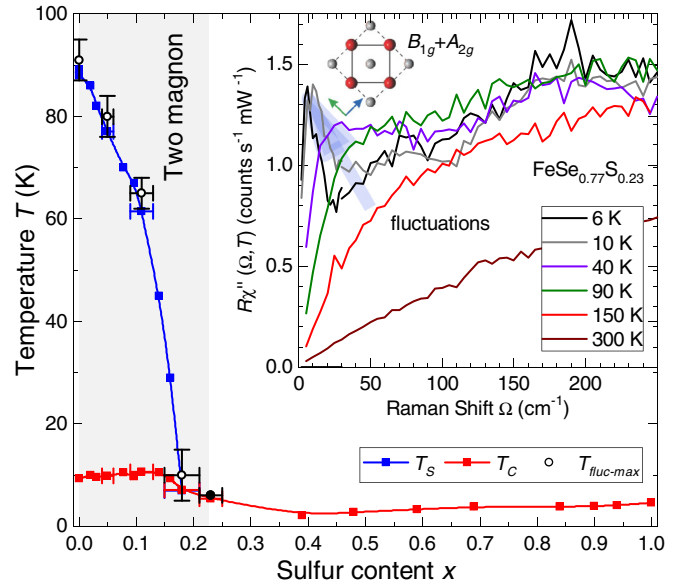

FIG. 5. Phase diagram of FeSe$_{1-x}$S$_x$ with $T_{\text{fluct,max}}$ tracing T_S in the region where the two-magnon feature was observed in the Raman scattering experiment. T_c taken from Ref. [15]. The full circle represents the lowest accessible temperature. Inset: Low-energy Raman spectrum showing the temperature dependence of the fluctuation contribution at $x = 0.23$. Spectra for all doping levels $0 \leqslant x \leqslant 0.23$ are shown in Fig. 8.

peak may be observed for $x = 0$ which continuously softens above the structural transformation at $T_s = 90$ K, fades away below T_s, and almost vanishes at 21 K [22,34]. The line shape and the temperature dependence above T_s can be described quantitatively in terms of critical fluctuations in a similar fashion as in Ba(Fe$_{1-x}$Co$_x$)$_2$As$_2$ [22,33,35]. For increasing doping, this extra intensity starts to develop at lower temperatures. However, remarkably enough the temperature where this peak's intensity is maximal, $T_{\text{fluct,max}}$, always coincides with the respective transition temperature $T_s(x)$. At $x = 0.23$ the fluctuation response gains intensity down to the lowest accessible temperatures as presented in the inset of Fig. 5. Thus, the phase transition line of the nematic phase can also be tracked by the Raman response. For $x = 0.33$ (the next available doping level) the fluctuation response cannot be observed any further. Concomitantly, the two-magnon excitation at 500 cm^{-1} becomes unobservable. The most likely explanation of this coincidence is that the two phenomena have the same origin and result from spin excitations. However, there is no consensus on that view in the literature, and Zhang *et al.* [36] and Chibani *et al.* [34] interpret the same experimental observation in terms of quadrupolar charge fluctuations. Yet, one certainly has to answer the question as to why the fluctuations are not found in the simulations [23].

Most probably, the length scale the simulations can deal with limits the applicability of the exact diagonalization method. Since it was intended to study the temperature dependence the cluster had to be sufficiently small (4×4) to keep the time for the simulations finite [23]. For the two-magnon excitations, the 4×4 cluster is sufficient because only nearest-neighbor spins are important. However, close to

the transition the correlation length of fluctuations diverges making them inaccessible for the small clusters tractable numerically. Actually, well above the transition there is a shoulder on the low-energy side of the two-magnon peak which may be associated with the fluctuations but the shoulder is lost close to T_s. Thus, although there are experimental arguments in favor of spin fluctuations at low energy there is no theoretical support for this conjecture.

The last question we wish to address concerns the origin of possible local or quasilocal spin order in $FeSe_{1-x}S_x$ for $x < 0.3$. It was observed a while ago that the width of the various bands derived from the orbitals close to the Fermi surface varies by approximately a factor of 3 or more. There are itinerant yz and xz bands crossing the Fermi surface at E_F and a weakly dispersing xy band just below E_F [29] on which the nearly localized spins may reside [30,32]. It is an important question to which extent the fluctuations at low energy are related to these spins. As a matter of fact, Ba122 displays itinerant SDW magnetism as manifested by a gap and a coherence peak along with fluctuations [22,33], whereas FeSe exhibits signatures of local spins and also fluctuations at low energies as shown here. In $FeSe_{1-x}S_x$ both phenomena disappear together above $x > 0.23$.

IV. CONCLUSION

Raman results covering the entire substitution range $0 \leqslant x \leqslant 1$ in $FeSe_{1-x}S_x$ were presented. The main goal was the study of the physics around the QCP where the nematic instability approached zero transition temperature in the range $0.16 \leqslant x \leqslant 0.23$. We find a striking signature of this transition in both the phonon and the electronic spectra. Whereas the B_{1g} phonon varies continuously with S substitution, the A_{1g} phonon and all structures in the xx spectra show a discontinuity above $x = 0.23$. Similarly, the electronic spectra dominated by spin excitations change abruptly here. Both the two-magnon excitations and the low-energy fluctuations disappear. We argue that they are interrelated. Since we could not observe gap excitation for $x > 0$, statements about the evolution of the superconducting pairing are currently not possible. Another issue is the exact position of the quantum critical transition and its sharpness.

APPENDIX A: PHONON DISPERSION AND DENSITY OF STATES

We have performed density functional theory (DFT) calculations as implemented in the ABINIT package [38]. We have used the Perdew-Burke-Ernzerhof functional tailored for solids [39] and optimized norm-conserving pseudopotentials [40,41], where Fe $3s^2 3p^6 3d^6 4s^2$, S $3s^2 3p^4$, and Se $3d^{10} 4s^2 4p^4$ are treated as valence electrons. The energy cutoff for the plane-wave basis was set to 50 Ha. The lattice parameters and atomic positions used in the calculations were directly obtained from our x-ray diffraction measurements (performed at 300 K). Following previous first-principles studies on phonons in, for example, FeS [18], the crystal structures were not further relaxed, to achieve optimal characterization of the phonon frequencies. Here, both FeS and FeSe adopt the simple tetragonal space group $P4/nmm$ (No. 129), where Fe occupies Wyckoff position $2a$ and S/Se position $2c$. The latter comprises an additional degree of freedom, namely, the height of the chalcogen atoms S and Se with respect to the Fe plane, denoted as z. An overview of the lattice parameters that were used in the calculations is provided in Table I.

Subsequently, the phonon dispersions were obtained from density functional perturbation theory (DFPT) calculations, also within ABINIT. Here, we have used a $15 \times 15 \times 9$ k-point grid for the electron wave vectors and a $5 \times 5 \times 3$ q-point grid for the phonon wave vectors. For the electronic occupation we employed Fermi-Dirac smearing with broadening factor $\sigma = 0.01$ Ha.

The results of these calculations are shown in Fig. 6. FeS is found to have phonon frequencies stretching up to 344 cm^{-1} [Fig. 6(a)], which is significantly higher than the maximum phonon value of 273 cm^{-1} obtained for FeSe [Fig. 6(b)], owing to the higher atomic mass of Se compared to S. The atom-resolved phonon densities of states (DOS) of both compounds reveal a mixture of iron and chalcogen contribution throughout the entire phonon spectrum [Figs. 6(c) and 6(d)]. Interestingly, there is a change of dominant phonon character, with the lower modes dominated by Fe in FeS, while the lower modes have predominant Se character in FeSe. This reversal can be understood from the fact that the atomic number of Fe ($Z = 26$) lies in between those of S ($Z = 16$) and Se ($Z = 34$). These differences in atomic masses lead moreover

TABLE I. Lattice parameters, obtained from x-ray diffraction measurements, used in the DFT and DFPT calculations.

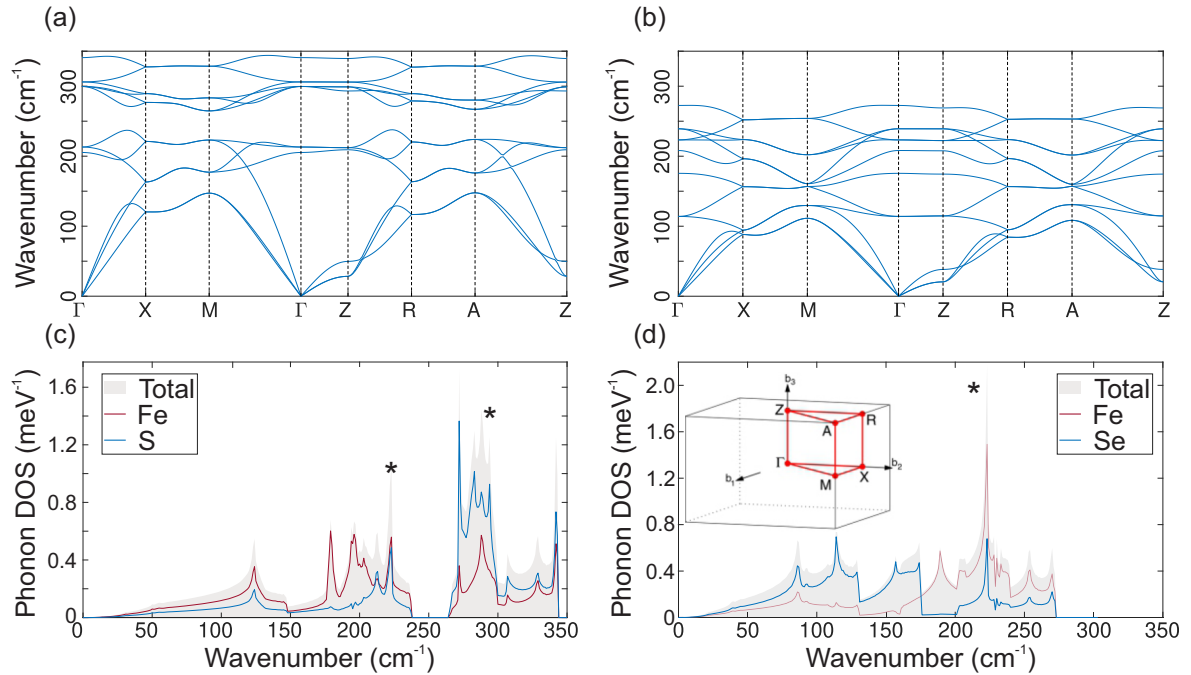| Compound	a (Å)	c (Å)	z (units of c)
FeS	3.6795	5.0321	0.2578
FeSe	3.7707	5.5202	0.2671

FIG. 6. Calculated phonon band structures of (a) FeS and (b) FeSe. Phonon DOS of (c) FeS and (d) FeSe, including partial contributions from Fe and S/Se. The Brillouin zone of both structures depicted in black is shown in the inset of (d), with the irreducible Brillouin zone, along which the band structures are plotted, in red [37]. The energies of the extra peaks in Fig. 7 are also indicated here by asterisks.

to a small energy gap between Fe- and S-dominated modes in FeS (between 238 and 265 cm^{-1}), which is entirely absent in FeSe.

APPENDIX B: FeSe$_{0.52}$S$_{0.48}$ AND FeS

For convenience we show here additional doping levels in Fig. 7. The spectrum for $x = 1$ in panel (b) was already published elsewhere [18]. Note that for $x'x'$ both A_{1g}^{ph} and B_{1g}^{ph} are projected and that the labels for the symmetry-forbidden peaks P3 and P4 are different from those in the earlier paper [18]. $x = 0.48$ [Fig. 7(a)] is in the middle between FeSe and FeS, and one can therefore expect the strongest contribution from defect-induced scattering. This interpretation is supported by the presence of structures in both configurations. All peaks resolved at $x = 0.69$ in xx configuration are also observed here. In addition there are two lines marked by asterisks which appear only at $x = 0.48$. Since they appear also for $x'x'$ we interpret them in terms of contributions from the PDOS as shown in Fig. 6 where the respective energies correspond to a high DOS of either FeSe or FeS. Structure P5 may be related to the high-energy part of FeS.

APPENDIX C: FLUCTUATION RESPONSE

The Raman response from fluctuations was studied by various authors [22,36,42]. While the experiments agree by and large, the interpretation is still controversial. Here we show that the fluctuations appear along with the two-magnon excitations at approximately 500 cm^{-1} from a frustrated spin system [22,23]. Above $x = 0.23$ we could neither observe fluctuations nor two-magnon excitations (see Fig. 4). We cannot entirely exclude that the fluctuations are masked by in-

sufficient stray-light rejection in the more disordered samples but consider it unlikely.
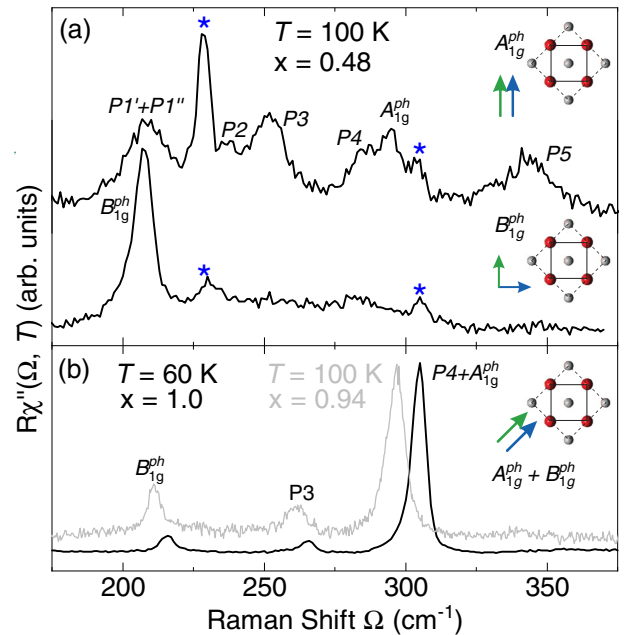
FIG. 7. FeSe$_{1-x}$S$_x$ for $x = 0.48$, $x = 0.94$, and $x = 1$. (a) A_{1g}^{ph} (xx) and B_{1g}^{ph} (xy) spectra for FeSe$_{0.52}$S$_{0.48}$. In addition to the phonons and the structures observed at the other doping levels there are two relatively sharp lines (marked by asterisks) which we associate with the PDOS. They may also arise from a nearly ordered superstructure close to 50% doping.
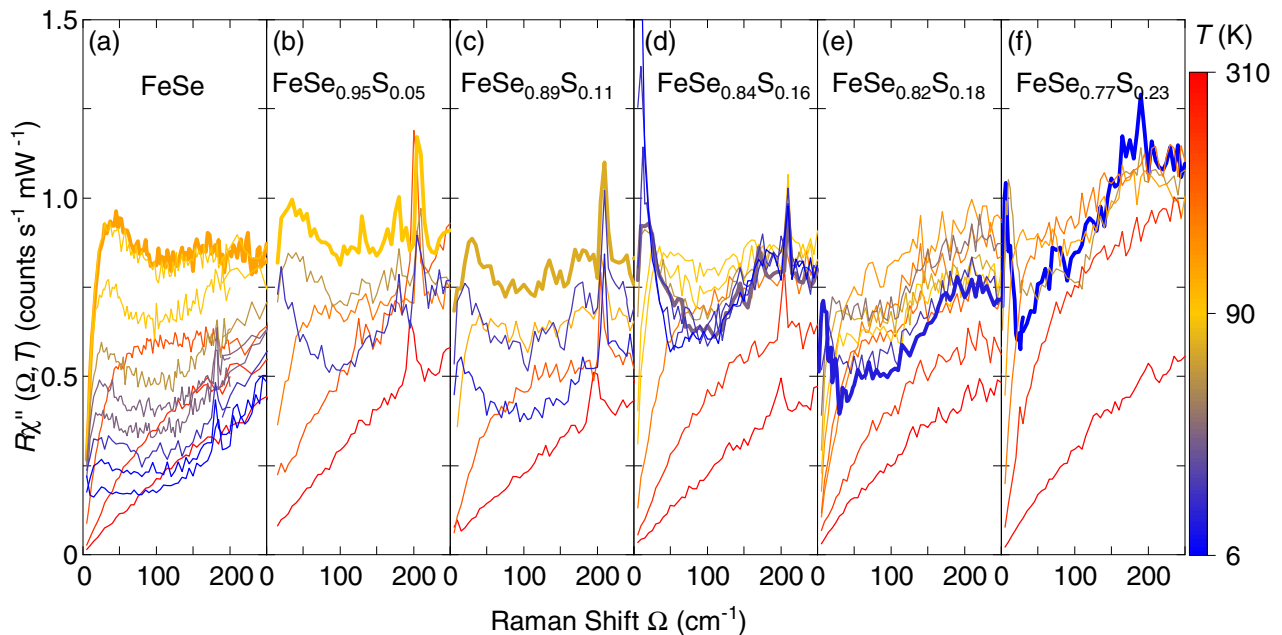
FIG. 8. Fluctuation response of FeSe$_{1-x}$S$_x$ for $0 \leqslant x \leqslant 0.23$. The spectra with the maximal intensity in the fluctuations are highlighted. The respective temperatures are (a) 91 K, (b) 80 K, (c) 65 K, (d) 25 K, (e) 10 K, and (f) 6 K, where 6 K was the lowest accessible temperature. The temperatures are compiled in Fig. 5 and track the transition to the nematic phase.

If excitations are very close to zero energy one encounters two difficulties: (1) The experimentally accessible quantity is the differential cross section, $d^2\sigma/(d\Omega\,d\omega) \propto S(q = 0, \omega)$. The dynamical structure factor or Van Hove function $S(q = 0, \omega)$ is related to the imaginary part of the Raman response function Im$\chi(q = 0, \omega)$ through the fluctuation-dissipation theorem as $S(q = 0, \omega) = \pi^{-1}\{1 + n(\omega, T)\}Im\chi(q = 0, \omega)$ [43]. The Bose factor $1 + n(\omega, T)$ increases rapidly towards $\omega = 0$ for $\hbar\omega < k_B T$ and conceals all spectral features below $k_B T$. Since the fluctuation-dissipation theorem is derived on purely statistical arguments the response function contains exactly the same information as the structure factor but makes features at low energy visible. Thus it is sensible to show Im$\chi(q = 0, \omega)$ rather than $S(q = 0, \omega)$. (2) If the surface is not atomically flat there is stray light from insufficient rejection of the laser. The problem is aggravated

when atoms of the residual gas accumulate on the surface at low temperature. In panels (a), (b), and (d) of Fig. 8 this effect can be observed. Fortunately, it can be distinguished from the desired response which always goes through zero linearly for causality reasons. (a) In FeSe only the spectra at 10 K show a slight increase which, however, is separated from the fluctuation peak at finite energy. (b) The increase at 10 K is partially resulting from stray light but the maximal intensity is already observed at 80 K. (c) There is little contribution from stray light. (d) Here the stray light becomes strong below 20 K. In (e) and (f) the stray light is negligible.

Remarkably, the overall intensity of all spectra is approximately the same, whereas the maximal intensity in the fluctuation peak is observed at different temperatures as indicated in Fig. 8. These temperatures compare well with the boundary of the nematic phase as shown in Fig. 5.

[1] D. J. Scalapino, A common thread: The pairing interaction for unconventional superconductors, Rev. Mod. Phys. **84**, 1383 (2012).

[2] E. Fradkin, S. A. Kivelson, and J. M. Tranquada, *Colloquium*: Theory of intertwined orders in high temperature superconductors, Rev. Mod. Phys. **87**, 457 (2015).

[3] S. Lederer, Y. Schattner, E. Berg, and S. A. Kivelson, Enhancement of Superconductivity near a Nematic Quantum Critical Point, Phys. Rev. Lett. **114**, 097001 (2015).

[4] A. E. Böhmer, T. Arai, F. Hardy, T. Hattori, T. Iye, T. Wolf, H. v. Löhneysen, K. Ishida, and C. Meingast, Origin of the Tetragonal-to-Orthorhombic Phase Transition in FeSe: A Combined Thermodynamic and NMR Study of Nematicity, Phys. Rev. Lett. **114**, 027001 (2015).

[5] T. M. McQueen, A. J. Williams, P. W. Stephens, J. Tao, Y. Zhu, V. Ksenofontov, F. Casper, C. Felser, and R. J. Cava, Tetragonal-to-Orthorhombic Structural Phase Transition at 90 K in the Superconductor Fe$_{1.01}$Se, Phys. Rev. Lett. **103**, 057002 (2009).

[6] M. D. Watson, T. K. Kim, A. A. Haghighirad, N. R. Davies, A. McCollam, A. Narayanan, S. F. Blake, Y. L. Chen, S. Ghannadzadeh, A. J. Schofield *et al.*, Emergence of the nematic electronic state in FeSe, Phys. Rev. B **91**, 155106 (2015).

[7] F.-C. Hsu, J.-Y. Luo, K.-W. Yeh, T.-K. Chen, T.-W. Huang, P. M. Wu, Y.-C. Lee, Y.-L. Huang, Y.-Y. Chu, D.-C. Yan, and M.-K. Wu, Superconductivity in the PbO-type structure α-FeSe, Proc. Natl. Acad. Sci. USA **105**, 14262 (2008).

[8] S. Medvedev, T. M. McQueen, I. A. Troyan, T. Palasyuk, M. I. Eremets, R. J. Cava, S. Naghavi, F. Casper, V. Ksenofontov, G. Wortmann, and C. Felser, Electronic and magnetic phase diagram of β-$Fe_{1.01}Se$ with superconductivity at 36.7 K under pressure, Nat. Mater. **8**, 630 (2009).

[9] Y. Sato, S. Kasahara, T. Taniguchi, X. Xing, Y. Kasahara, Y. Tokiwa, Y. Yamakawa, H. Kontani, T. Shibauchi, and Y. Matsuda, Abrupt change of the superconducting gap structure at the nematic critical point in $FeSe_{1-x}S_x$, Proc. Natl. Acad. Sci. USA **115**, 1227 (2018).

[10] X. Lai, H. Zhang, Y. Wang, X. Wang, X. Zhang, J. Lin, and F. Huang, Observation of superconductivity in tetragonal FeS, J. Am. Chem. Soc. **137**, 10148 (2015).

[11] U. Pachmayr, N. Fehn, and D. Johrendt, Structural transition and superconductivity in hydrothermally synthesized Fe*X* (*X* = S, Se), Chem. Commun. **52**, 194 (2016).

[12] N. Lazarević and R. Hackl, Fluctuations and pairing in Fe-based superconductors: Light scattering experiments, J. Phys.: Condens. Matter **32**, 413001 (2020).

[13] S. Holenstein, U. Pachmayr, Z. Guguchia, S. Kamusella, R. Khasanov, A. Amato, C. Baines, H.-H. Klauss, E. Morenzoni, D. Johrendt, and H. Luetkens, Coexistence of low-moment magnetism and superconductivity in tetragonal FeS and suppression of T_c under pressure, Phys. Rev. B **93**, 140506(R) (2016).

[14] F. K. K. Kirschner, F. Lang, C. V. Topping, P. J. Baker, F. L. Pratt, S. E. Wright, D. N. Woodruff, S. J. Clarke, and S. J. Blundell, Robustness of superconductivity to competing magnetic phases in tetragonal FeS, Phys. Rev. B **94**, 134509 (2016).

[15] A. Wang, A. Milosavljevic, A. M. M. Abeykoon, V. Ivanovski, Q. Du, A. Baum, E. Stavitski, Y. Liu, N. Lazarevic, K. Attenkofer *et al.*, Suppression of superconductivity and nematic order in $Fe_{1-y}Se_{1-x}S_x(0 \leqslant x \leqslant 1; y \leqslant 0.1)$ crystals by anion height disorder, Inorg. Chem. **61**, 11036 (2022).

[16] A. Wang, L. Wu, V. N. Ivanovski, J. B. Warren, J. Tian, Y. Zhu, and C. Petrovic, Critical current density and vortex pinning in tetragonal $FeS_{1-x}Se_x$ ($x = 0, 0.06$), Phys. Rev. B **94**, 094506 (2016).

[17] V. Gnezdilov, Y. G. Pashkevich, P. Lemmens, D. Wulferding, T. Shevtsova, A. Gusev, D. Chareev, and A. Vasiliev, Interplay between lattice and spin states degree of freedom in the FeSe superconductor: Dynamic spin state instabilities, Phys. Rev. B **87**, 144508 (2013).

[18] A. Baum, A. Milosavljević, N. Lazarević, M. M. Radonjić, B. Nikolić, M. Mitschek, Z. I. Maranloo, M. Šćepanović, M. Grujić-Brojčin, N. Stojilović *et al.*, Phonon anomalies in FeS, Phys. Rev. B **97**, 054306 (2018).

[19] M. Cardona and M. L. W. Thewalt, Isotope effects on the optical spectra of semiconductors, Rev. Mod. Phys. **77**, 1173 (2005).

[20] G. Turrell, *Infrared and Raman Spectra of Crystals* (Academic, London/New York, 1972).

[21] Y. Mizukami, M. Haze, O. Tanaka, K. Matsuura, D. Sano, J. Böker, I. Eremin, S. Kasahara, Y. Matsuda, and T. Shibauchi, Thermodynamics of transition to BCS-BEC crossover superconductivity in $FeSe_{1-x}S_x$, arXiv:2105.00739.

[22] A. Baum, H. N. Ruiz, N. Lazarević, Y. Wang, T. Böhm, R. Hosseinian Ahangharnejhad, P. Adelmann, T. Wolf, Z. V. Popović *et al.*, Frustrated spin order and stripe fluctuations in FeSe, Commun. Phys. **2**, 14 (2019).

[23] H. Ruiz, Y. Wang, B. Moritz, A. Baum, R. Hackl, and T. P. Devereaux, Frustrated magnetism from local moments in FeSe, Phys. Rev. B **99**, 125130 (2019).

[24] W. Spengler and R. Kaiser, First and second order Raman scattering in transition metal compounds, Solid State Commun. **18**, 881 (1976).

[25] F. Nabeshima, Y. Kawai, N. Shikama, Y. Sakishita, A. Suter, T. Prokscha, S. E. Park, S. Komiya, A. Ichinose, T. Adachi, and A. Maeda, Sulfur-induced magnetism in $Fese_{1-x}s_x$ thin films on $LaAlO_3$ revealed by muon spin rotation/relaxation, Phys. Rev. B **103**, 184504 (2021).

[26] X. Yi, X. Xing, L. Qin, J. Feng, M. Li, Y. Zhang, Y. Meng, N. Zhou, Y. Sun, and Z. Shi, Hydrothermal synthesis and complete phase diagram of $FeSe_{1-x}S_x(0 \leqslant x \leqslant 1)$ single crystals, Phys. Rev. B **103**, 144501 (2021).

[27] J. K. Glasbrenner, I. I. Mazin, H. O. Jeschke, P. J. Hirschfeld, R. M. Fernandes, and R. Valentí, Effect of magnetic frustration on nematicity and superconductivity in iron chalcogenides, Nat. Phys. **11**, 953 (2015).

[28] A. I. Coldea, Electronic nematic states tuned by isoelectronic substitution in bulk $FeSe_{1-x}S_x$, Frontiers Phys. **8**, 594500 (2021).

[29] M. Yi, Z.-K. Liu, Y. Zhang, R. Yu, J.-X. Zhu, J. Lee, R. Moore, F. Schmitt, W. Li, S. Riggs *et al.*, Observation of universal strong orbital-dependent correlation effects in iron chalcogenides, Nat. Commun. **6**, 7777 (2015).

[30] Z. P. Yin, K. Haule, and G. Kotliar, Kinetic frustration and the nature of the magnetic and paramagnetic states in iron pnictides and iron chalcogenides, Nat. Mater. **10**, 932 (2011).

[31] K. M. Stadler, Z. P. Yin, J. von Delft, G. Kotliar, and A. Weichselbaum, Dynamical Mean-Field Theory Plus Numerical Renormalization-Group Study of Spin-Orbital Separation in a Three-Band Hund Metal, Phys. Rev. Lett. **115**, 136401 (2015).

[32] S. L. Skornyakov, V. I. Anisimov, D. Vollhardt, and I. Leonov, Effect of electron correlations on the electronic structure and phase stability of FeSe upon lattice expansion, Phys. Rev. B **96**, 035137 (2017).

[33] F. Kretzschmar, T. Böhm, U. Karahasanović, B. Muschler, A. Baum, D. Jost, J. Schmalian, S. Caprara, M. Grilli, C. Di Castro *et al.*, Critical spin fluctuations and the origin of nematic order in $Ba(Fe_{1-x}Co_x)_2As_2$, Nat. Phys. **12**, 560 (2016).

[34] S. Chibani, D. Farina, P. Massat, M. Cazayous, A. Sacuto, T. Urata, Y. Tanabe, K. Tanigaki, A. E. Böhmer, P. C. Canfield *et al.*, Lattice-shifted nematic quantum critical point in $FeSe_{1-x}S_x$, npj Quantum Mater. **6**, 37 (2021).

[35] U. Karahasanovic, F. Kretzschmar, T. Böhm, R. Hackl, I. Paul, Y. Gallais, and J. Schmalian, Manifestation of nematic degrees of freedom in the Raman response function of iron pnictides, Phys. Rev. B **92**, 075134 (2015).

[36] W. Zhang, S. Wu, S. Kasahara, T. Shibauchi, Y. Matsuda, and G. Blumberg, Quadrupolar charge dynamics in the nonmagnetic $FeSe_{1-x}S_x$ superconductors, Proc. Natl. Acad. Sci. USA **118**, e2020585118 (2021).

[37] W. Setyawan and S. Curtarolo, High-throughput electronic band structure calculations: Challenges and tools, Comput. Mater. Sci. **49**, 299 (2010).

[38] X. Gonze, B. Amadon, G. Antonius, F. Arnardi, L. Baguet, J.-M. Beuken, J. Bieder, F. Bottin, J. Bouchet, E. Bousquet *et al.*, The ABINIT project: Impact, environment and recent developments, Comput. Phys. Commun. **248**, 107042 (2020).

[39] J. P. Perdew, A. Ruzsinszky, G. I. Csonka, O. A. Vydrov, G. E. Scuseria, L. A. Constantin, X. Zhou, and K. Burke, Restoring the Density-Gradient Expansion for Exchange in Solids and Surfaces, Phys. Rev. Lett. **100**, 136406 (2008).

[40] D. R. Hamann, Optimized norm-conserving Vanderbilt pseudopotentials, Phys. Rev. B **88**, 085117 (2013).

[41] M. van Setten, M. Giantomassi, E. Bousquet, M. Verstraete, D. Hamann, X. Gonze, and G.-M. Rignanese, The PseudoDojo: Training and grading a 85 element optimized norm-conserving pseudopotential table, Comput. Phys. Commun. **226**, 39 (2018).

[42] P. Massat, D. Farina, I. Paul, S. Karlsson, P. Strobel, P. Toulemonde, M.-A. Méasson, M. Cazayous, A. Sacuto, S. Kasahara *et al.*, Charge-induced nematicity in FeSe, Proc. Natl. Acad. Sci. USA **113**, 9177 (2016).

[43] L. D. Landau and E. M. Lifshitz, *Electrodynamics of Continuous Media* (Pergamon, Oxford, 1960), p. 377.